Food Chemistry 442 (2024) 138383

Contents lists available at ScienceDirect

Food Chemistry

journal homepage: www.elsevier.com/locate/foodchem

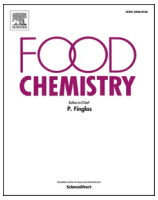

Sensitive dual-signal detection and effective removal of tetracycline antibiotics in honey based on a hollow triple-metal organic framework nanozymes

Qing Chen [a,1], Hongjin Zhang [b,1], He Sun [b], Yuanzhen Yang [b], Dandan Zhang [a], Xin Li [c], Lei Han [d], Guannan Wang [a,*], Yang Zhang [a,*]

[a] School of Pharmacy, Shenyang Medical College, 146 Huanghe North Avenue, Shenyang 110034, China
[b] School of Basic Medicine, Shenyang Medical College, 146 Huanghe North Avenue, Shenyang 110034, China
[c] Department of Science and Technology, Shenyang Medical College, 146 Huanghe North Avenue, Shenyang 110034, China
[d] College of Chemistry and Pharmaceutical Sciences, Qingdao Agricultural University, 700 Changcheng Road, Qingdao 266109, Shandong, China

ARTICLE INFO

Keywords:
Food analysis
Nanozymes
Dual-signal detection
Antibiotics
Metal–organic framework

ABSTRACT

In this work, a colorimetric/fluorescent dual-signal mode sensor is proposed for the sensitive, selective and accurate detection and removal of tetracycline antibiotics (TCs). A triple-metal MOF of NiCoFe is successfully synthesized and controllable adjusted the shape of the hollow structure for the first time, and then modified with TCs aptamer. The as-prepared triple-atom MOF (*apt*-NiCoFe-MOF-74) exhibits well-defined hollow morphology, high crystallinity, and high surface areas endow their alluring adsorption and removal performances for TCs. More attractively, this triple-metal MOF show a good peroxidase-like activity and strong fluorescence property at 540 nm of *apt*-NiCoFe-MOF-74 when excitation wavelength was 370 nm. Inspire by this, a dual-signal output biosensor is constructed and the linear absorbance response is well correlated with wide range and low LOD for TCs. The biosensor provided an universal method with satisfactory sensitivity and accuracy for TCs analysis in real food samples.

1. Introduction

Tetracycline antibiotics (TCs) involving in tetracycline, oxytetracycline, chlorotetracy cline, and doxycycline are a type of broad- spectrum antibiotic can effectively inhibit the spread of bacteria like gram-negative bacteria and gram-positive bacteria (Gan et al., 2021; Gao et al., 2023; J. Li et al., 2023; Z. Xu et al., 2023; S. Zhang, Sun, Liu, Li, Wang, & Chen, 2022). Due to their efficiency, low cost, good oral absorption and other advantages, they has been widely applied in aquaculture, medicine, and stockbreeding as a feed growth promoter (Wang et al., 2020). In recent years, the misuse of TCs has caused their accumulation in the environment, which can be ingested by humans through food and water, posing a threat to human health (Khezerlou, Tavassoli, Alizadeh Sani, Ghasempour, Ehsani, & Khalilzadeh, 2023; Mohammed Ameen, Qasim, Alhasan, Hama Aziz, & Omer, 2023; D. Xu et al., 2023; H. Yang et al., 2021). Additionally, the overuse of TCs can lead to bacterial resistance to antibiotics, disrupting the balance of the ecosystem. To address this issue, various strategies have been developed to detect TCs, such as high-performance liquid chromatography-mass spectrometry (HPLC-MS) (Pang, Lv, Sun, Yang, & Shen, 2021; Zhu, Wang, Sun, & Zhou, 2013), surface enhanced Raman scattering (SERS) (H. Li et al., 2017; Bing Liu et al., 2022; Trong Duc, Thi Hue, & The Binh, 2022), antibacterial screening tests (Falsafi, Mobasheri, Nariman, & Najafi, 2004), and enzyme-linked immunosorbent assay (ELISA) (Du et al., 2019; Yulan Zhang, Lu, Liu, Zhao, & Xi, 2007). However, these methods often require complex sample preparation, specialized and costly instruments, and specialized skills, making them difficult to use in routine TCs testing. Among them, both the fluorescent sensor and colorimetric sensor were regarded as a potential method of antibiotics detection with the advantages of simple operation, low cost, high sensitivity and selectivity, etc (Mohammed Ameen, Sher Mohammed, & Omer, 2023; Y. Yang et al., 2020). However, these single-signal sensors as the quantitative signal can be affected by surroundings and complex matrix interference, resulting in false positive results. Recently, the dual-signal

* Corresponding authors.
E-mail addresses: chemwangguannan@126.com (G. Wang), zhangyang@symc.edu.cn (Y. Zhang).
[1] These authors contributed equally to this work.

https://doi.org/10.1016/j.foodchem.2024.138383
Received 8 November 2023; Received in revised form 26 December 2023; Accepted 4 January 2024
Available online 10 January 2024

mode sensing system has been gaining traction as a novel detection strategy in biosensor design and application, offering an array of advantages such as increased detection dimensionality, more measurement data, and improved sensitivity and accuracy (N. Liang et al., 2022; Rong et al., 2023; Shi et al., 2023; L. Yang et al., 2024). Fluorescent/colorimetric dual-mode sensing platforms have been explored in the previous reports, but the detection results are vulnerable to interference from the sample matrix due to the lack of specificity in the design of dual-mode response probes. In addition, integrating the detection and removal of TCs into a platform to realize the effect of "two birds with one stone" remains a challenge.

Nanozymes, which possess enzyme-like features, have gained a lot of attention lately as they can address the issues associated with traditional enzymes, for instance, variability, high cost of preparation, and limited practical applications (Huang, Ren, & Qu, 2019; Wu et al., 2019; D. Zhang et al., 2023). It has been discovered that these enzymes possess an intrinsic horseradish peroxidase (HRP)-mimicking ability, allowing them to oxidize chromogenic substances like ophenylenediamine (OPD), 3,3′,5,5′-tertamethylbenzidine, and diazoaminobenzene. This makes them ideal for biosensing applications. (Jiang, Ni, Rosenkrans, Huang, Yan, & Cai, 2019; X. Liang & Han, 2020; Zandieh & Liu, 2023). However, most of their activities are still far lower than that of natural enzymes. Currently, many works interested in investigating that how to enhance the catalytic performance of nanozymes comprise of surface alteration (Biwu Liu & Liu, 2017), morphological control (Xie, Yang, Zhang, Guo, Chen, & He, 2021), shrinking the size of nanomaterials (Bing, Sun, Wang, Song, & Ren, 2018), and heteroatom doping (Jiao et al., 2020). Surface alteration can protect the active sites of the catalyst and reduce the atom usage. Reducing the size of nanozymes can improve the surface free energy, which can result in material accumulation and deactivation. Among these, heteroatom doping has become a significant tactic to enhance the catalytic activity for further meet the actual requirement, however, only a very few studies in recent years, as far as we know, have investigated the enzyme-like properties of multi-metal nanozymes. Furthermore, The nanozymes with a hollow structure which not only provides a large specific surface area, but also has a containment effect, thus resulting in improved catalytic efficiency and mass transfer of substrates.

Intrigued by the merits on nanozymes, a novel fluorescent NiCoFe-doped triple-metal nanozymes with Ni, Co and Fe three atom sites coordinated with dioxidoterephthalate was designed and controllable synthesized for the first time to selectively and sensitively detect TCs. The modified aptamer and the remarkable peroxidase (POD)-like activity of *apt*-NiCoFe-MOF-74 endow specific colorimetric detection capacity toward TCs, and the metals in triple-metal organic frameworks provide unsaturated sites to recognize TCs. Together with fluorescence property of *apt*-NiCoFe-MOF-74, a targeted fluorescent/colorimetric sensor were developed toward to the TCs in real sample. Additionally, the hollow nanoarchitecture contributes high surface area, and meanwhile enhances mass transfer and mitigates the diffusion barrier, which remarkably enhances the adsorption and removal capacity for TCs.

2. Experiment

2.1. Materials and reagent

All chemicals of reagent grade were commercially available and used without further purification. The single-strand 76 mer DNA aptamer was custom synthesized with 5′-end amino modification (Mw (23 747.43), $K_d = 63.6$ nM) by Sangon Biotech Co., Ltd. (Shanghai, China), with the following sequence: 5′-CGTACGGAATTCGCTAGCCCCCCGGCAGGCCACGGC TTGGGTTGGTCCCACTGCGCGTGGATCCGAGCTCCACGTG-3′. Aptamers were dissolved in ultrapure water at a concentration of 100 mM. tetracycline (TET), doxycycline (DOX), chlortetracycline (CTC), streptomycin (STR), oxytetracycline (OTC), gentamicin (GEN), chloramphenicol (CHL), erythromycin (ERY), cephalosporin (CEP) and sulfadimidine (SMD), terephthalic acid (TA) and hydroethidine (HE) were all obtained from Sigma Aldrich Co., Ltd. Glycine (Gly), Lysinne (Lys), Histidine (His), Arginine (Ary), Tryptophan (Try), Methionine (Met), Phenylalanine (Phe), Alanine (Ala) and Glucose (Glu) and inorganic salts were purchased from Sinopharm Chemical Reagent Co. Ltd. (China). 2,5-Dihydroxyterephthalic acid (H_4DOT, $\geq$ 98.0 %) was purchased from Energy Chemical. Cobaltous nitrate hexahydrate ($Co(NO_3)_2{\cdot}6H_2O$, 99.99 %), Nickel (II) nitrate hexahydrate ($Ni(NO_3)_2{\cdot}6H_2O$, 98 %), Iron (III) nitrate nonahydrate ($Fe(NO_3)_3{\cdot}9H_2O$, 98.5 %), hexadecyltrimethylammonium bromide (CTAB), sodium hydroxide (NaOH), hydrogen peroxide (H_2O_2, 30 %), acetic acid and analytically purity grade salts used for preparation of buffers were purchased from Sinopharm Chemical Reagent Co. Ltd. (China). 3,3,5,5-tetramethylbenzidine (TMB) used in the experiments was from TCI (Shanghai, China). N, *N*-dimethylformamide (DMF), ethanol, acetone, were analytical grade (AR) and obtained from Energy Chemical Company. All aqueous solutions used were prepared with the ultrapure water (>18 MΩ cm) prepared by a Millipore system.

2.2. Physical methods

XRD measurements were carried out with a Bruker D8 Adance X-ray diffractometer using Cu Kα1 radiation, with a scanning range between 5° and 80° using a scan step of 5° min-1 to check the phase purity. The morphology andmicrostructure of the materials were recorded through transmission electron microscopy (TEM, TalosF200X) and scanning electron microscopy (SEM, JEM-2100F). Dynamic light scattering (DLS) was tested using Zetasizer Nano-ZS instrument (Malvern, UK). The chemical composition was investigated using an ESCALab250 electron spectrometer (Thermo Scientific Corporation) with monochromatic 150 W Al Kα radiations. The fluorescence analysis was performed onfluorescence spectrophotometer F-7000 (Hitachi, Japan).

2.3. Synthesis of NiCoFe-MOF-74

H_4DOT (0.39 g, 2 mmol), $Fe(NO_3)_3{\cdot}9H_2O$ (0.73 g, 1.8 mmol), $Co(NO_3)_2{\cdot}6H_2O$ (0.55 g, 1.8 mmol), and $Ni(NO_3)_2{\cdot}6H_2O$ (0.55 g, 1.8 mmol) were added ina mixture of DMF (75 mL), EtOH (5 mL) and H_2O (5 mL), which was marked as standard solution. Then the standard solution (A) was sealed into a Teflon-lined stainless steel container and heated at 120 °C for 24 h. After reaction isfinished and cooled down to the room temperature, materials (named as FeCoNi-MOF-74) were washed with acetone three times, dried at 60 °C in vacuum.

2.4. Synthesis and hollow apt-NiCoFe-MOF-74

Different with the synthesis of NiCoFe-MOF-74 (ESI 1.3), hollow NiCoFe-MOF-74 was firstly achieved by the addition of acetic acid (100 μL) and CTAB (100 mg) to the standard solution (A) (ESI 1.3) and keeping at 120 °C for 24 h. the pre-product experienced the same handling method of washing, centrifuging and drying as well as 2.2 and the production named as *h*-NiCoFe-MOF-74 were washed with acetone three times, dried at 60℃ in vacuum. *h*-NiCoFe-MOF-74 was subsequently anchored with an TCs-aptamer with 3′-end amino modification. Typically, 6 mg of *h*-NiCoFe-MOF-74 was dispersed in a 3 mL PEI aqueous solution (20 mg mL^{-1}, pH 8.5) followed by 18 mL TCs-aptamer (100 mM) and 1 mL PBS (10 mM, pH 7.4) were added, and the mixture was vibrated for 4 h at room temperature. The final product *apt*-NiCoFe-MOF-74 was purified via centrifugation at 1×10^4 rpm for 5 min, followed by washing with PBS (10 mM, pH 7.4), the final product was store at 4℃ for further usage.

2.5. POD-like activity analysis of apt-NiCoFe-MOF-74

The colorimetric reaction was used to study POD-like activity of *apt*-NiCoFe-MOF-74. To this end, 100 μL of 0.054 M TMB solution and 50 μL

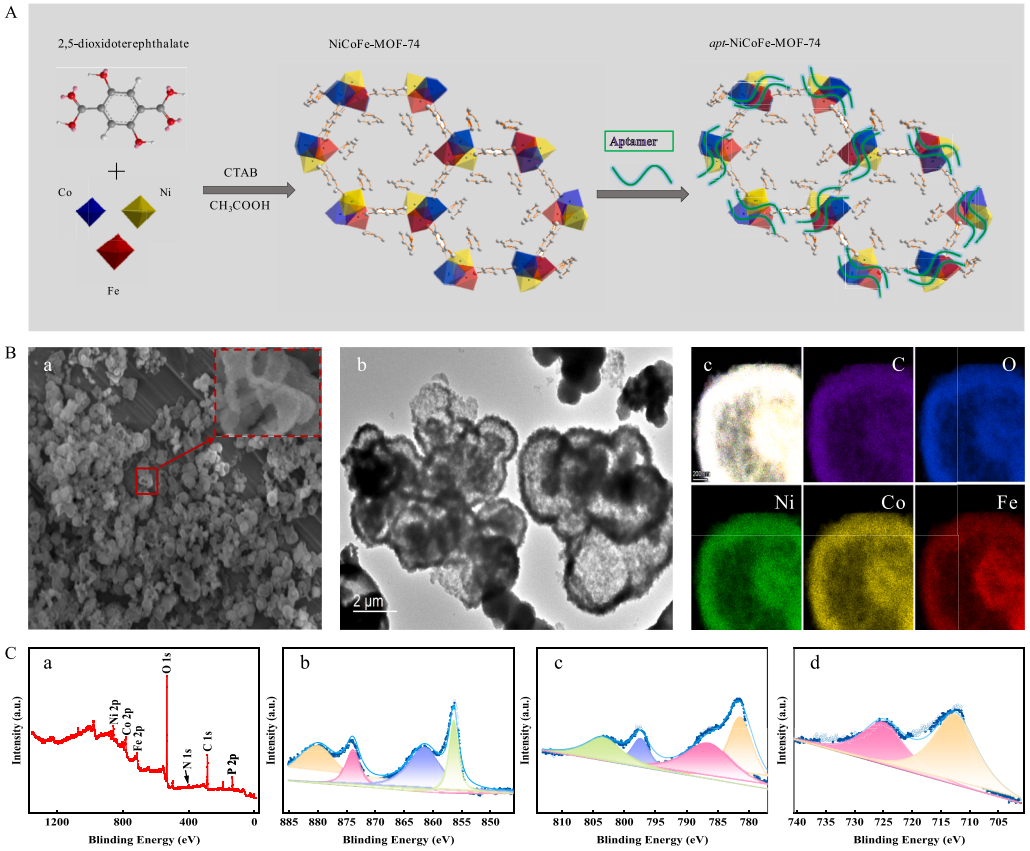

Fig. 1. (A) The preparation of *apt*-NiCoFe-MOF-74. (B) SEM image (a), HR-TEM image (b), and corresponding elemental mappings (c) of *apt*-NiCoFe-MOF-74, showing the hierarchical elemental distributions of Ni, Co and Fe. (C) XPS spectra of *apt*-NiCoFe-MOF-74 (a), and high-resolution spectra of Ni 2p (b), Co 2p (c) and Fe 2p (d).

of 5 mM H_2O_2 were mixed in a NaAc-HAc buffer with pH 4.0. Subsequently, 7 μL of 5 mg mL^{-1} dispersion of *apt*-NiCoFe-MOF-74 was added and the mixture was agitated at room temperature for 30 min. The absorbance of the solution was then measured at 652 nm. Additionally, the effect of pH, temperature and reaction time on the POD-like activity was also studied.

The steady-state kinetic assay were carried out in NaAc-HAc buffer (0.1 M, pH 4.0), involving in 7 μL *apt*-NiCoFe-MOF-74 (5 mg mL^{-1}), as the initial concentration of either TMB (0.2–3 mM) or H_2O_2 (0.05–2 mM) was established under the aforementioned optimized conditions (pH = 4, T = 37 °C).

The absorbance at 652 nm of the resultant solution was recorded. The typical *Michaelis-Menten* curves were obtained and the kinetic parameters were caculate by the *Lineweaver-Burk* plot: $V = V_{max}$ [*S*] / (K_m + [*S*]), where *V*, V_{max}, [*C*] and K_m represent the initial reaction velocity, the maximal velocity, the concentration of substrate (TMB or H_2O_2) and *Michaelis* constant, respectively.

2.6. Catalytic mechanism

To discuss the catalytic mechanism of *apt*-NiCoFe-MOF-74 POD-like activity, scavengers of TA was used to eliminate •OH. 10 mM TA were added to an acetate buffer (pH 4.5) containing 0.5 mM TMB and 2.0 mM H_2O_2. Fluorescence spectrum was recorded with an excitation wavelength of 315 nm.

2.7. Colorimetric detection of TCs

Typically, different concentrations of TCs solution (10 μM to 1000 μM) was added into the buffer solution (pH = 4) consisting of *apt*-NiCoFe-MOF-74 (100 μg mL^{-1}), TMB (1 mM) and H_2O_2 (1 mM) to maintain the total volume at 600 μL, and the mixed system reacted for 15 min, and the absorbance at 652 nm was recorded. Meanwhile, the resultant solution was analyzed by above method without modified TCs-aptamer under the same conditions as control. The effects of general ions, amino acids, glucose and other antibiotics on TCs detection were also investigated. In the selective and anti-interference experiments, the concentration of interfering substance was the 2-fold concentration of TCs, except antibiotics were equal concentration of TCs. All experiments were performed in parallel three times.

2.8. Fluorescence detection of TCs

To optimize detection conditions, 10 mg *apt*-NiCoFe-MOF-74 was dispersed in 10 mL H_2O, and sonicated to make it completely disperses to obtain a stock solution with a concentration of 1 mg mL^{-1}. Both of the effects of pH values from 3 to 10 and incubationtime (0–30 min) on the detection property of *apt*-NiCoFe-MOF-74 were investigated. Under the optimal conditions, the *apt*-NiCoFe-MOF-74 stock solution (50 μL) was added into TCs solutions with different concentrations (0–25 mg/L), then diluted to 2 mL with buffer solution (pH 4.0). After incubating for 10 min, the fluorescent emission spectra were recorded from 550 nm to 750 nm at λ_{ex} = 370 nm. The method of selective and anti-interference experiments are same as the section 2.7. All experiments were performed in parallel three times. The detection property was test by the quenching efficiency (Q_E (%)), which is described by equation (1).

$$Q_E(\%) = \frac{F_0 - F}{F_0} \times 100 \quad (1)$$

where F_0 and *F* are the FL intensity of the *apt*-NiCoFe-MOF-74 before and

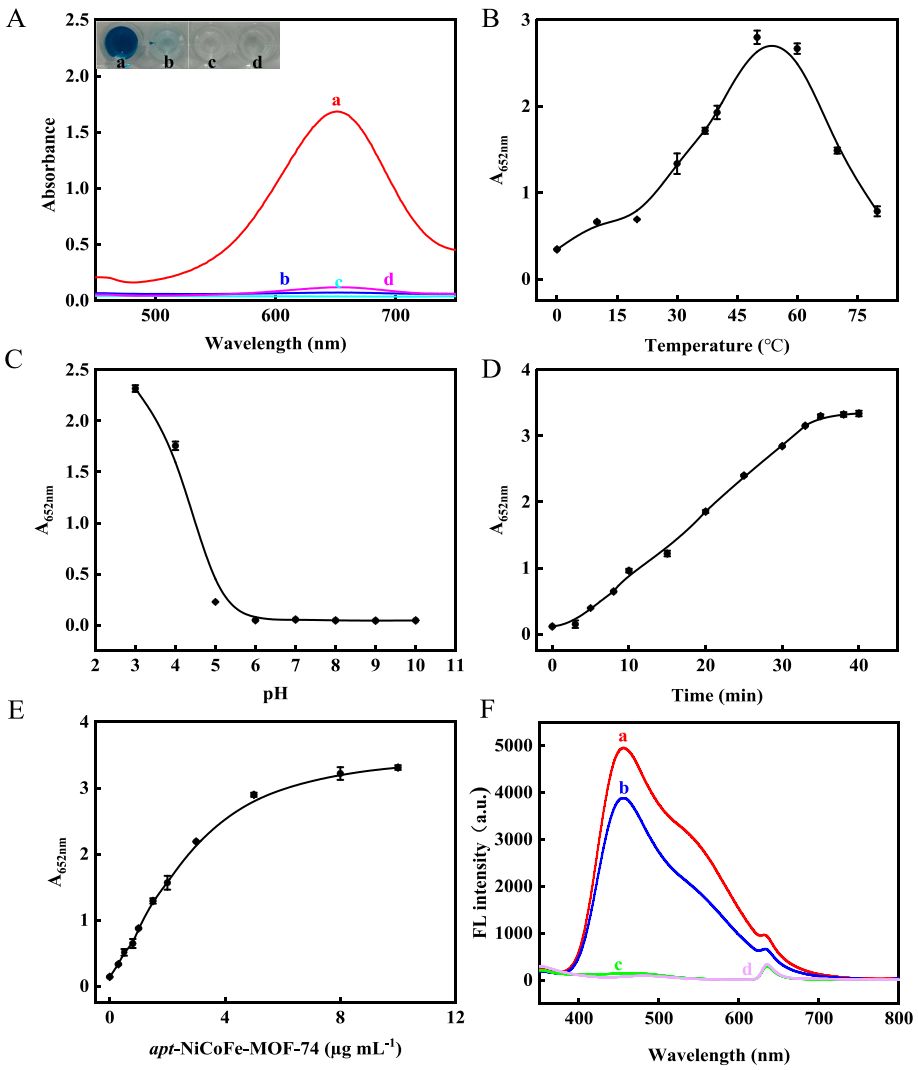

Fig. 2. (A) POD-like activity: typical absorption spectra of TMB, oxidationcatalyzed by *apt*-NiCoFe-MOF-74 and control groups in the presence of H_2O_2 at pH 4.0, and corresponding color changes (inset (a): *apt*-NiCoFe-MOF-74 + H_2O_2 + TMB + Buffer), (b): TMB + H_2O_2, (c): TMB + *apt*-NiCoFe-MOF-74, (d): H_2O_2 + *apt*-NiCoFe-MOF-74). (B) The effect of temperature (0 °C to 80 °C), (C) pH 3–10, (D) reaction time (0–40 min) and (E) concentration of *apt*-NiCoFe-MOF-74 on the POD-like activity. (F) Fluorescent spectra of TA after reaction with H_2O_2 in the absence and presence of *apt*-NiCoFe-MOF-74. Concentration of *apt*-NiCoFe-MOF-74 was 2.5 μg mL^{-1}, H_2O_2 was 10 mM and TMB was 0.5 mM.

after TCs introduction, respectively.

2.9. Adsorption studies of TCs

The performance of *apt*-NiCoFe-MOF-74 on these four TCs adsorption was evaluated, respectively, as the pH was adjusted to 3–8 with 0.1 M NaOH or HCl. The adsorption kinetics was investigated by adding 0.2 g/L *apt*-NiCoFe-MOF-74 to TCs solution (50 mg/L) with different incubation times, and UV–Vis spectra was recorded to determine the residual TCs concentration of the supernatant. The adsorption capacity was studied by adding 0.2 g/L *apt*-NiCoFe-MOF-74 to TCs solution with different initial concentrations. The adsorption capacity was calculated by the following equation (2) and (3):

$$Q^* = \frac{Q_m - b \pm \sqrt{b^2 - 4ac}}{2a} \tag{2}$$

$$Q^* = \frac{Q_m \times C_e}{K_d + C_e} \tag{3}$$

where C_e (mg/L) represents TCs concentration, Q^* (mg g^{-1}) is the amount of adsorbed TCs at equilibrium, Q_m (mg g^{-1}) denotes the adsorption capacity and K_d is the dissociation constant.

The pseudo-first-order (PFO) and pseudo-second-order (PSO) models were described by Equation (4) and Equation (5):

$$\ln(Q_e - Q_t) = \ln Q_e - k_1 t \tag{4}$$

$$\frac{t}{Q_t} = \frac{t}{Q_e} + \frac{1}{k_2 Q_e^2} \tag{5}$$

where Q_t (mg g^{-1}) and Q_e (mg g^{-1}) represent the adsorption capacity at any time t (min) and the equilibrium adsorption capacity of analytes. k_1 (1/min) is the equilibrium rate constant of the pseudo first-order sorption and k_2 (g/mg/min) is the equilibrium rate constant of the pseudo second-order sorption.

The fitting equations of the *Langmuir* model and *Freundlich* model were shown in *Equation* (6) and *Equation* (7), respectively.

$$\frac{C_e}{Q_e} = \frac{1}{Q_m k_L} + \frac{C_e}{Q_m} \tag{6}$$

$$\ln Q_e = \ln k_F + \frac{1}{n} \ln C_e \tag{7}$$

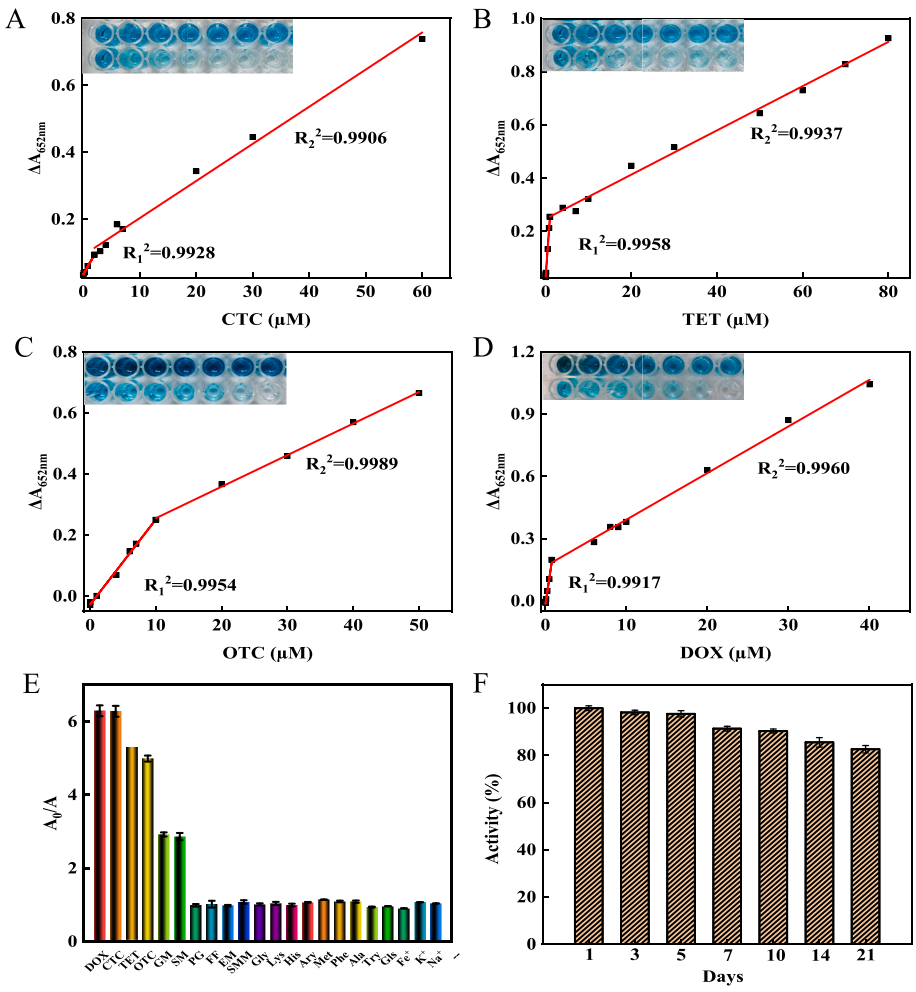

Fig. 3. The linear calibration plots for the quantitative determination of CTC (A), TET (B), OTC (C), DOX (D). ($\Delta A = A_0$-A, where A_0 and A are the absorbance of the reaction system without and with CTC, TET, OTC and DOX). (E) Selectivity determination of *apt*-NiCoFe-MOF-74 colorimetric sensor for four antibiotics. (F) The stability of POD-like activities for *apt*-NiCoFe-MOF-74 three weeks.

2.10. Detection of TCs in real food samples

To further investigate the practical value of this dual-signal sensor, the recovery of the actual sample was detected by colorimetric and fluorescence sensors, respectively. We chose three kinds of honey (lime tree honey, robinia honey and loquat honey) as the actual sample for detection. The honey samples experienced simple diluted ten times with buffer solution (pH 4.0) and filtered by filter 0.22 μm membrane without any other processing. Using the standard addition method, various honey samples possessing different concentrations of four TCs were prepared and used for colorimetric and fluorescent measurement.

3. Results and discussion

3.1. Characterization

The synthesis of NiCoFe-MOF-74 began with the mixing of divalent metals (Ni^{2+}, Co^{2+}, Fe^{2+}) with DOT in a dimethyl formamide/ethanol/water solution, and the incorporation of cationic surfactants CTAB and acetic acid with a pre-specified concentration (Fig. 1A). This was completed by a 24 h solvent thermal crystallization at 120℃. Following, the morphology and element distribution of *apt*-NiCoFe-MOF-74 were characterized. The SEM (Fig. 1B) and TEM images (Fig. 1C) showed that the *apt*-NiCoFe-MOF-74 had a typical hollow porous structure with uniform size. The EDS mapping images showed a homogeneous distribution of Ni, Co and Fe throughout the carbon frame (Fig. 1D). The Ni, Co, Fe, C, O content in the nanozyme was 9.29, 9.53, 8.93, 26.4 and 45.85 at%, respectively, according to the EDS analysis. To obtain further insight into the constituent elements and chemical states of the *apt*-NiCoFe-MOF-74, X-ray photoelectron spectroscopy (XPS) analyses were carried out. In the survey spectrum of the composites (Fig. 1E), the main constituments of C, O, N, P, Ni, Co, Fe were found in the *apt*-NiCoFe-MOF-74, which were from aptamer and NiCoFe-MOF-74, respectively. This was consistent with the results of elemental composition in EDX imaging. The X-ray Photoelectron Spectroscopy (XPS) results of *apt*-NiCoFe-MOF −74 revealed the presence of divalent metal ions, such as Ni^{2+}, Co^{2+}, and Fe^{2+}. The Fe 2p spin orbitals were observed at two core-level peaks, centered at 712.5 and 725.1 eV (Fig. 1F). The high-resolution Co 2p XPS spectrum showed two binding energy peaks at 786.6 and 797.5 eV, which corresponded to Co 2p 3/2 and Co 2p 1/3 ground states, as well as shakeup satellite peaks at 803.8 eV (Fig. 1G). The Ni 2p XPS spectrum exhibited peaks at 873.8 and 856.1 eV, corresponding to Ni 2p 3/2 and Ni 2p 1/2, along with shakeup satellite peaks at 861.4 and 879.7 eV (Fig. 1H). X-ray diffraction (XRD) pattern of the *apt*-NiCoFe-MOF-74 showed two distinct main sharp characteristic diffraction peaks with different intensities at $2\theta = 6.8°$ and $2\theta = 11.9°$, which were consistent with simulated MOF-74 crystalline structure (Fig. S1). These characteristic may be attributed to the presence of different orientations in the lattice, leading to a non-uniform spatial distribution of organic ligands and metal ions within the crystal, thus resulting in the two distinct diffraction peaks. Furthermore, the N_2

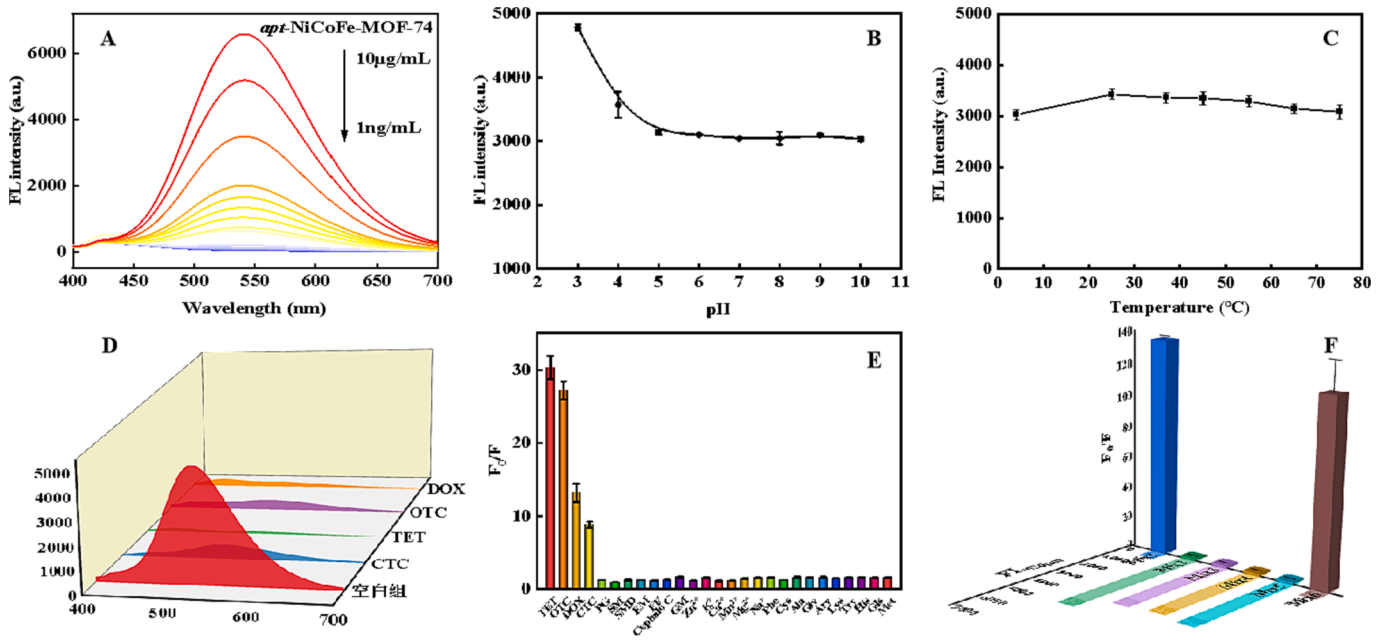

Fig. 4. (A) The FL intensity of *apt*-NiCoFe-MOF-74 range from 1.0 ng mL^{-1} to 10 μg mL^{-1}. FL intensity of *apt*-NiCoFe-MOF-74 at different pHs (B) and temperatures (C). (D) Fluorescence spectra of *apt*-NiCoFe-MOF-74 (2.5 mg/L) with adding four TCs (267 mM) under optimized conditions (pH 4.0, T = 25℃). (E) FL intensity response of *apt*-NiCoFe-MOF-74 to 0.25 mM four TCs and interfering species in the absence of TCs. (F) FL intensity response of *apt*-NiCoFe-MOF-74 to the corresponding mixture of interfering substances. (Mix 1: four TCs; Mix 2: other antibiotics except TCs; Mix 3: amino acids; Mix 4: various ions; Mix 5: all the interfering substances; Mix 6: all the interfering substances + four TCs).

adsorption–desorption isotherms recorded further indicated the porous characteristics of the *apt*-NiCoFe-MOF-74 (Fig. S2). The isotherms exhibited characteristics for micropores and mesopores, and the *apt*-NiCoFe-MOF-74 exhibited a typical IV isotherm with an H4-type hysteresis loop and *Brunauer-Emmett-Teller* (BET) specific surface areas was 619 m^2 g^{-1}, which was also demonstrated the porous structures of NiCoFe-MOF-74 remained after controlled modification of aptamer. The successful modification of the aptamer on NiCoFe-MOF-74 was confirmed by the FTIR measurements. Fig. S3 presented FTIR spectra of NiCoFe-MOF-74 and *apt*-NiCoFe-MOF-74. The phosphate group of aptamer was found to be successfully modified on the surface of NiCoFe-MOF-74, as evidenced by emerging the antisymmetric and symmetric stretching vibrations at 1260 and 1036 cm^{-1}, respectively. Besides, the asymmetric vibrations and symmetric vibrations of carboxylate groups was observed at 1560 cm^{-1} and 1413 cm^{-1}. The peak at 585 cm^{-1} may be attributed to the vibration between the metal and functional groups after modified aptamer. Thus, it can be concluded that NiCoFe-MOF-74 was successfully synthesized and aptamer was modified prospectively.

3.2. POD-like activity of apt-NiCoFe-MOF-74

The catalytic oxidation properties of *apt*-NiCoFe-MOF-74 were explored by testing the capacity to oxidize typical substrates. Using TMB as a chromogenic substrate, the POD-like activity of *apt*-NiCoFe-MOF-74 was evaluated in a nitrogen atmosphere. The results showed that *apt*-NiCoFe-MOF-74 could catalyze the oxidation of colorless TMB into blue oxidized TMB (oxTMB) in the existence of H_2O_2, with the maximum absorbance centered at 652 nm (Fig. 2A) and the catalytic oxidation property was not affected by aptamer modification (Fig. S4). Furthermore, it was found that the POD-like activity of *apt*-NiCoFe-MOF-74 was affected by temperature, pH, reaction time and concentrations (Fig. 2B-E). The optimal conditions for *apt*-NiCoFe-MOF-74 were determined to be 50 °C and pH 4.0, displaying excellent POD-like activity even in acidic conditions. Contrarily, H_2O_2 tended to decompose at alkaline conditions and a higher temperature, leading to a reduction of the absorbance in the catalytic system.

To investigate the catalytic mechanism, TA and HE was employed to verify the generation of •OH and $•O^{2-}$ during the catalytic reaction. On one hand, strong fluorescent compounds 2-hydroxy terephthalic acid (TAOH) could generate as TA react with •OH at the emission wavelength of 430 nm. In Fig. 2F, it was found obvious fluorescent signal centered at 430 nm for TA + H_2O_2 + *apt*-NiCoFe-MOF-74 group. It indicated that the proposed the nanozyme catalyzed decomposition of H_2O_2 to produce •OH in comparison of the control groups. On the other hand, HE was utilized as a specific probe for $•O^{2-}$, enabling the tracking of $•O^{2-}$ to produce ethidium with a strong fluorescence emission at approximately 590 nm. Despite the increased concentration of *apt*-NiCoFe-MOF-74, there was no apparent change in fluorescence for the POD-like activity, indicating that $•O^{2-}$ was not generated (Fig. S5).

The catalytic reaction rate of *apt*-NiCoFe-MOF-74 increased with the increasing concentration of substrate TMB and H_2O_2 until reaching a plateau, indicating that the catalytic reaction followed the *Michaelis-Menten* kinetics (Fig. S6A and B). By analyzing the *Line weaver-Burk* plot, it was observed that the *Michaelis-Menten* constant (K_m) for TMB substrate was 0.35 (Fig. S6C) and 0.45 for H_2O_2 substrate (Fig. S6D). The lower K_m value indicated a superior affinity and higher catalytic activity between the *apt*-NiCoFe-MOF-74 and the substrates.

3.3. Colorimetric detection of TCs

Under optimal conditions, a linear calibration curve was generated based on the absorbance change at 652 nm when concentration of four antibiotics ranged from 0.05 to 80 μM with LOD was 6 nM for TET (Fig. 3A), 0.01 to 50 μM with LOD was 10 nM for OTC (Fig. 3B), 0.01 to 60 μM with LOD was 49 nM for CTC (Fig. 3C), 0.05 to 40 μM with LOD was 2.8 nM for DOX (Fig. 3D) according to the 3σ rule, respectively. The superior POD properties of *apt*-NiCoFe-MOF-74 contributed to its sensitivity in comparison of other nanozyme materials (Table S1). The selectivity of the *apt*-NiCoFe-MOF-74 hybrid system was also tested with 1 mM concentrations of general metal ions and biological molecules (Fig. 3E). Only a visible absorbance change was seen when 100 μM AA was present, suggesting that the colorimetric assay is highly selective

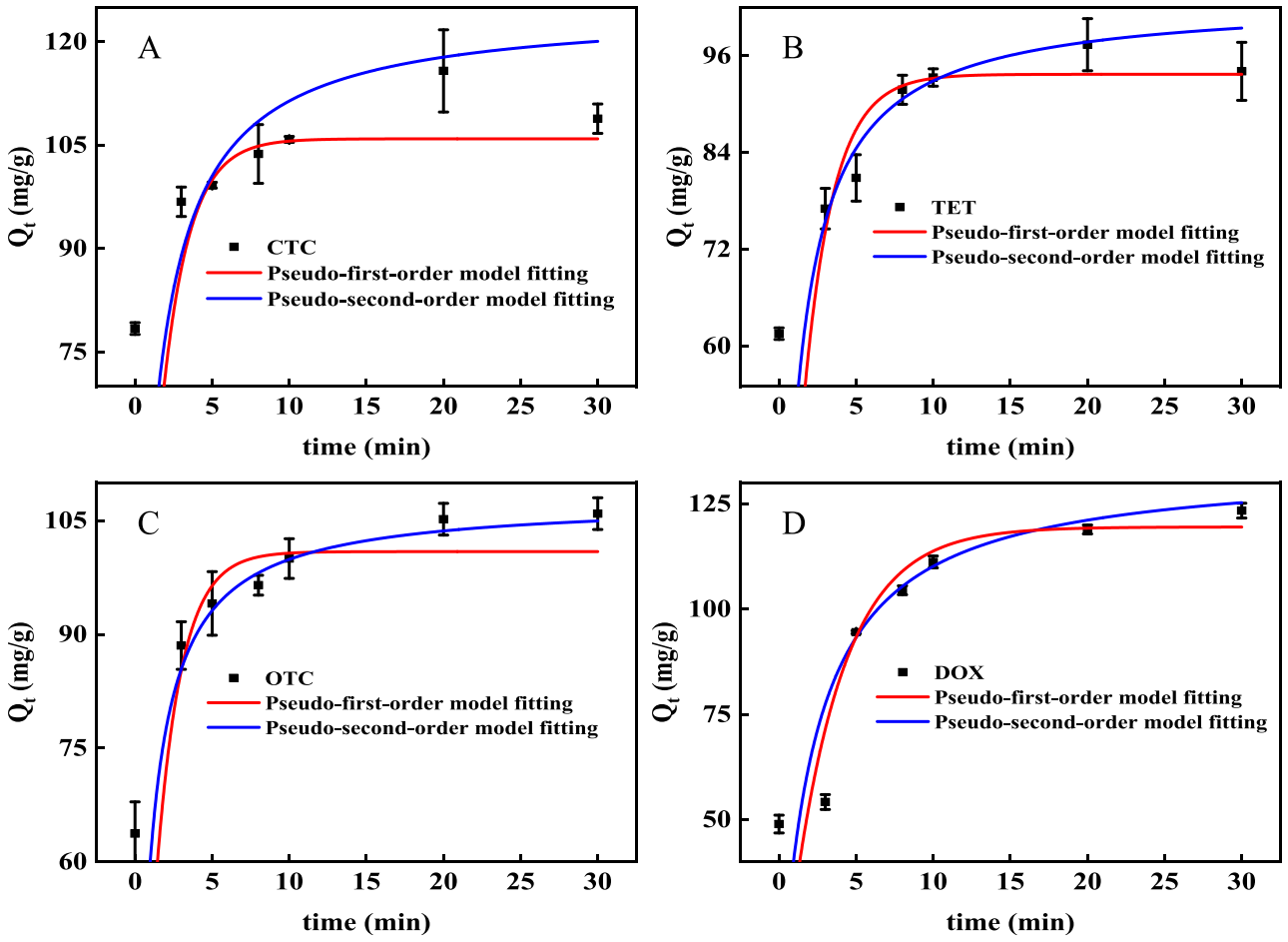

Fig. 5. Effect of the contact time on the four antibiotics adsorption including CTC (A), TET (B), OTC (C) and DOX (D) fitted by using pseudo-second-order and pseudo-first-order kinetic models.

and unaffected by interfering substances. Further, the selectivity assay was also performed in NiCoFe-MOF-74 without aptamer modification (Fig. S7), and the poor selectivity was observed to TCs, indicating auxiliarily the main special recognition between the *apt*-NiCoFe-MOF-74 and TCs attributed to the aptamer. Moreover, the catalytic stability of *apt*-NiCoFe-MOF-74 revealed that its catalytic activity was reduced by only 20 % after three weeks (Fig. 3F), demonstrating its relatively high stability.

3.4. Fluorescence (FL) determination of TCs

To investigate the capability of *apt*-NiCoFe-MOF-74 in selective detecting four antibiotics, we firstly explored the effects of concentration (1.0 ng mL^{-1} —10 μg mL^{-1}), pH (3.0–10.0), and temperature (4-75℃) on the fluorescence performance of the *apt*-NiCoFe-MOF-74. As results, the as-prepared *apt*-NiCoFe-MOF-74 generated strong fluorescence and the fluorescence intensity at 530 nm gradually increased with increasing concentrations from 1 ng mL^{-1} to 10 μg mL^{-1} (Fig. 4A). Under the optimized conditions (pH 4.0, T = 25℃) (Fig. 4B and C, corresponding fluorescence spectra were provided in Fig. S8 A and B), the stock four antibiotics standard solutions of CTC, TET, OTC and DOX were successively added to the detection system (5 μg mL^{-1} nanozyme, pH 4.0). After interaction for 15 min at room temperature, the FL intensity at 530 nm was recorded at an excitation wavelength of 370 nm. Fig. 4D showed the FL spectra in the presence of four antibiotics. As expected, FL intensities of *apt*-NiCoFe-MOF-74 at 530 nm gradually decreased with the incremental concentration of TCs. Following above experiments, the detection properties of the *apt*-NiCoFe-MOF-74 fluorescence sensor for four TCs were evaluated under optimal sensing conditions. As shown in Fig. S9, the fluorescence intensity at 530 nm exhibited a good linear relationship with the concentration of CTC from 2 nM to 100 μM ($y = 26.026x + 49.416$, $R^2 = 0.9951$), TET from 0.5 nM to 70 μM ($y = 42.156x + 10.449$, $R^2 = 0.9949$), OTC from 0.5 nM to 100 μM ($y = 36.200x + 31.167$, $R^2 = 0.9909$) and DOX from 1 nM to 90 μM ($y = 28.297x + 64.405$, $R^2 = 0.9930$). The limit of detection (LOD) of *apt*-NiCoFe-MOF-74 fluorescence sensor for CTC, TET, OTC and DOX was calculated to be 5.5 nM, 1.3 nM, 1.4 nM, 3.0 nM, respectively (Corresponding fluorescence spectra were shown in Fig. S10). The above results indicated that the *apt*-NiCoFe-MOF-74 had the potential for sensitive and quantitative detection of TCs. In Table S2 and S3, in comparison to other analytical methods and diverse fluorescence probes for detecting TCs, the as-prepared *apt*-NiCoFe-MOF-74 exhibited a wider detection range and lower LOD. To analyze the practicality of the *apt*-NiCoFe-MOF-74 fluorescence sensor for TCs, the selectivity and interference resistance was tested. A variety of substances such as amino acids, metal ions, other antibiotics (K^+, Na^+, Fe^{2+}, Gly, Lys, His, Ary, Try, Met, Phe, Ala and Glu). As shown in Fig. 4E, F and Fig. S11 A, B, the fluorescence intensity exhibited a clear change in the presence of TCs, while other antibiotics and substances showed negligible influence or little decreased upon the addition of these substances, indicating that these interfering substances had little to no effect on the sensing of TCs. These results showed that the fluorescent sensor was highly selective to resist interference and favorable sensitive for four TCs detection.

To further investigate the fluorescent sensor mechanism, the absorption spectra of four TCs and fluorescence spectra of as-prepared *apt*-NiCoFe-MOF-74 were determined and recorded in Fig. S12. The

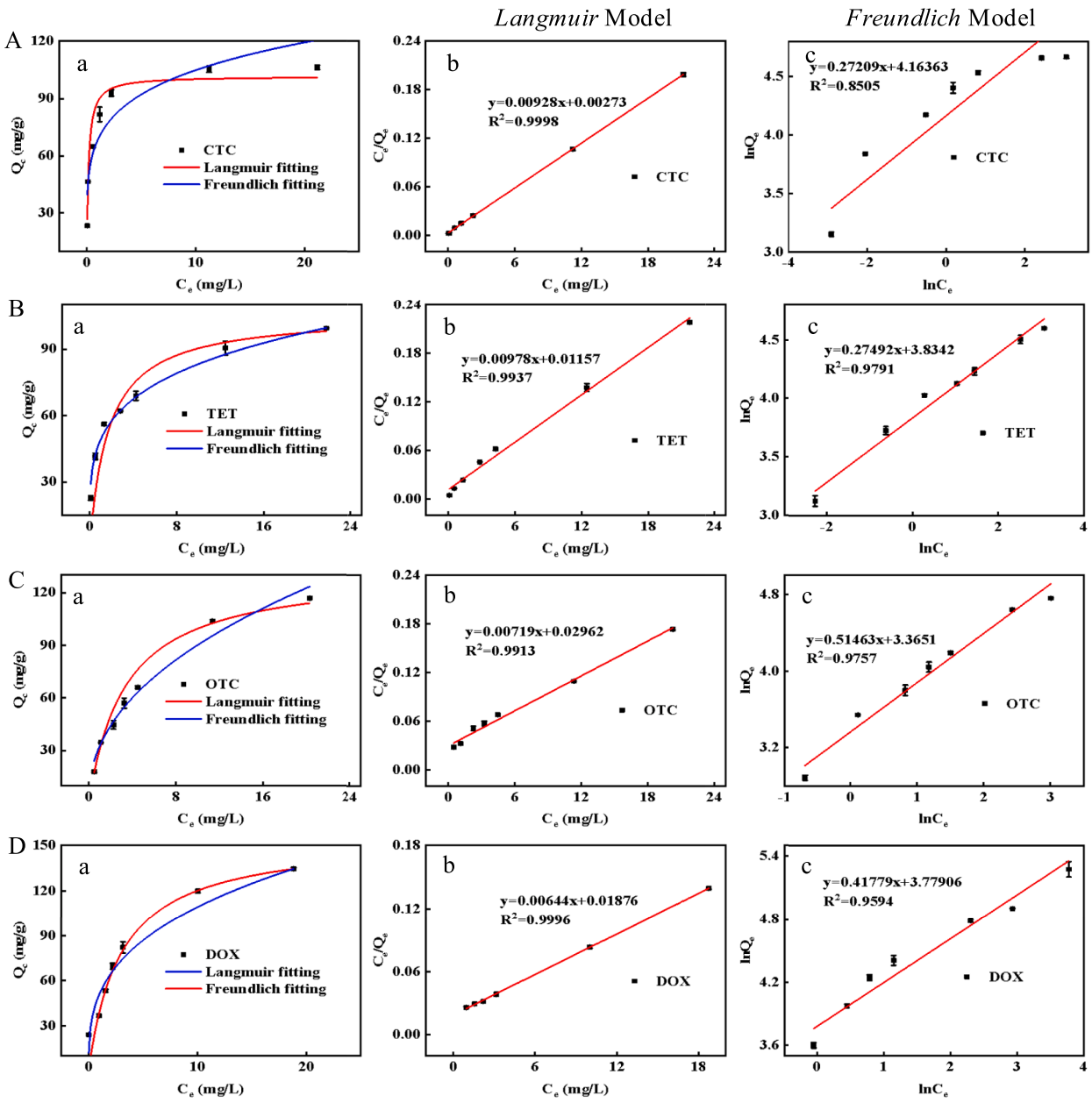

Fig. 6. Effect of the four antibiotics concentration on the adsorption and the corresponding nonlinear forms of *Langmuir* and *Freundlich* model for CTC (A), TET (B), OTC (C) and DOX (D).

fluorescence spectra of the as-prepared *apt*-NiCoFe-MOF-74 showed negligible overlap with the UV–vis spectra of the four TCs, ruling out the possibility of fluorescence resonance energy transfer (FRET) (Sapsford, Berti, & Medintz, 2006). However, the absorption spectra of the TCs significantly overlapped with the excitation spectra of *apt*-NiCoFe-MOF-74, which suggested that the intense absorption of the TCs greatly inhibited the absorption of excitation energy by *apt*-NiCoFe-MOF-74, leading to a significant FL quenching. The relevant inner-filter effect (IFE) was caculated by following *equation* (8):

$$\frac{F_{corr}}{F_{obsd}} = \frac{2.3dA_{ex}}{1-10^{-dA_{ex}}} \bullet \frac{2.3sA_{em}10^{gA_{em}}}{1-10^{-sA_{em}}} \tag{8}$$

where F_{obsd} and F_{corr} represent the maximum FL intensity measured and corrected after removing the IFE, respectively. A_{ex} and A_{em} are the absorbance of the detection system at wavelengths of 330 nm and 425 nm, respectively, d is thewidth of the cuvette (1.00 cm), s indicates the thickness of the excitation beam (0.10 cm), and g represents the distance from the excitation beam edge to the cuvette (0.40 cm).

The relevant correction factor (*CF*) is summarized in Table S4. It could be calculated the quenching efficiency from the IFE were 23 %, 25 %, 27 %, 29 % for CTC, TET, OTC and DOX, respectively. These demonstrated that the IFE was the main driving force leading to fluorescence quenching.

3.5. Adsorption experiments of TCs

The adsorption ability of *apt*-NiCoFe-MOF-74 toward four antibiotics was further investigated. The effect of pH (Fig. S13A) and contact times (Fig. S13B) for four antibiotics adsorption were recorded. Under the optimized condition (pH = 4.0, Time: 10 min), the adsorption kinetics of four antibiotics on the *apt*-NiCoFe-MOF-74 were studied to examine the effect of adsorption time. The results showed that the adsorption rate initially increased rapidly due to the abundance of adsorption sites on

Table 1
Recovery test and precision of the determination of TCs in real samples by colorimetric sensor.

TCs	Honeys	Spiked (μM)	Found (μM)	Recovery (%)	RSD (%, n = 3)
CTC	robinia honey	0.25	0.24	100.21	1.47
		2.5	2.55	103.86	2.94
		25	19.07	94.57	1.54
	loquat honey	0.25	0.26	106.15	2.94
		2.5	2.80	112.35	2.54
		25	24.01	96.047	0.67
	linden honey	0.25	0.27	108.70	3.89
		2.5	2.45	98.34	2.54
		25	24.17	96.71	1.11
TET	robinia honey	0.25	0.21	95.21	4.59
		2.5	2.25	90.22	3.00
		25	23.28	93.13	2.71
	loquat honey	0.25	0.18	91.18	4.59
		2.5	2.63	105.26	3.01
		25	21.95	87.81	0.60
	linden honey	0.25	0.18	92.18	4.59
		2.5	2.33	93.23	3.00
		25	26.31	105.26	0.30
OTC	robinia honey	0.25	0.19	91.10	2.81
		2.5	1.88	95.50	2.78
		25	26.86	107.46	0.48
	loquat honey	0.25	0.21	96.74	4.81
		2.5	2.77	110.84	4.81
		25	21.96	89.87	0.73
	linden honey	0.25	0.21	90.74	4.81
		2.5	2.77	110.84	4.81
		25	19.27	97.10	0.96
DOX	robinia honey	0.25	0.19	90.45	2.73
		2.5	2.60	104.10	0.27
		25	24.36	97.47	0.15
	loquat honey	0.25	0.20	91.27	4.18
		2.5	2.54	101.64	2.73
		25	23.91	95.64	0.27
	linden honey	0.25	0.20	92.19	2.73
		2.5	2.50	100.27	0.27
		25	25.23	100.94	0.15

Table 2
Recovery test and precision of the determination of TCs in real samples by fluorescent sensor.

TCs	Honeys	Spiked (μM)	Found (μM)	Recovery (%)	RSD (%, n = 3)
CTC	robinia honey	0.25	0.24	99.2	0.68
		2.5	2.82	113.4	1.13
		25	24.80	94.7	0.69
	loquat honey	0.25	0.24	99.7	1.36
		2.5	2.77	111.1	0.41
		25	24.45	97.8	0.97
	linden honey	0.25	0.26	104.1	0.67
		2.5	2.75	110.0	0.45
		25	24.76	99.0	0.25
TET	robinia honey	0.25	0.26	107.4	0.37
		2.5	2.525	101.3	0.24
		25	25.06	100.2	1.88
	loquat honey	0.25	0.25	102.9	6.51
		2.5	2.55	102.4	0.93
		25	24.60	98.4	0.76
	linden honey	0.25	0.26	106.4	1.36
		2.5	2.435	97.4	0.43
		25	23.83	95.3	4.58
OTC	robinia honey	0.25	0.24	100.3	0.47
		2.5	2.82	112.8	0.63
		25	24.71	98.9	0.19
	loquat honey	0.25	0.23	95.9	0.80
		2.5	2.66	106.6	3.19
		25	24.72	98.9	0.40
	linden honey	0.25	0.23	93.1	1.13
		2.5	2.72	108.9	0.80
		25	24.59	98.4	1.28
DOX	robinia honey	0.25	0.21	85.8	1.34
		2.5	2.51	106.6	3.93
		25	25.33	101.4	1.31
	loquat honey	0.25	0.25	102.2	1.77
		2.5	2.502	100.1	3.28
		25	25.03	100.2	1.70
	linden honey	0.25	0.24	99.2	3.44
		2.5	2.59	103.8	0.99
		25	25.09	100.4	0.28

the *apt*-NiCoFe-MOF-74, but then decreased and reached equilibrium within 10 min (Fig. 5A-D). To further analyze the adsorption kinetics, the pseudo-first- orderand pseudo-second-order kinetic models were employed, with the latter producing a better fit for CTC ($R^2 = 0.9983$), TET ($R^2 = 0.9982$), OTC ($R^2 = 0.9985$) and DOX ($R^2 = 0.9809$), and corresponding dynamic parameters were list in Table S5, which demonstrated that the adsorption process is chemisorption between TCs and the binding sites of the *apt*-NiCoFe-MOF-74 (Fig. S14A-D) (Z. Li, Xiao, Ge, & Koehler, 2015; Yang Zhang, Xing, Chen, & Wang, 2015).

The adsorption isotherm was also evaluated to determine the effect of the initial concentration of four antibiotics on *apt*-NiCoFe-MOF-74. The *Langmuir* and *Freundlich* isotherm models were used to describe the adsorption mechanism. It can be seen that the *Langmuir* model fitting the data better for all four antibiotics (Fig. 6), and the according parameters for the adsorptions were list in Table S6. These further implied that the adsorption process was chemical monolayer adsorption. By fitting the experimental data to *Langmuir* adsorption model, adsorption capacity of 109.8, 102.1, 107.2 and 131.1 mg g^{-1} for CTC, TET, OTC and DOX was derived, which agreed with the actual adsorption capacity of 115.6, 97.4, 105.2, 114.7 mg g^{-1}. As results, the *apt*-NiCoFe-MOF-74 has a relatively high adsorption capacity. It is worth noting that the existence of coexisting ions in the actual food samples. Therefore, two times concentrations of coexisting ions were added to the mixture of four TCs to assess the influence of interfering substance. As a result in Fig. S15, the *apt*-NiCoFe-MOF-74 had satisfactory anti-interference ability and could be applied to effectively remove the four TCs in the actual food samples.

3.6. Stability and reusability of apt-NiCoFe-MOF-74

Generally, the reusability and stability of the proposed *apt*-NiCoFe-MOF-74 are of great significance in practical applications. Therefore, the reusability, resorption experiments were conducted. As results, the fluorescence intensity of *apt*-NiCoFe-MOF-74 was still maintained above 85 % after five cycles (Fig. S16). Furthermore, adsorption capacity of *apt*-NiCoFe-MOF-74 were still at 80.2 %, 78.2 %, 78.9 % and 77.9 % for CTC, TET, OTC and DOX after five cycles, respectively (Fig S17). Additionally, take TET as model TCs to evaluate the material maintained

structural stability before and after adsorption of TCs. As shown in Fig. S18A and B, its still maintained the original shape before and after adsorption of TET, which demonstrated its structural stability.

3.7. Detection of real samples

To assess the reliability of the *apt*-NiCoFe-MOF-74 as a dual-signal sensor involving in colorimetric and fluorescence sensor, commercially available three types of honey were selected as actual samples to detect four kinds of TCs by the standard addition method. As results, the recoveries of colorimetric sensor were obtained from 94.57 to 112.35 % for CTC with RSD less than 3.89 %, 87.8 to 105.2 % for TET with RSD less than 3.1 %, 89.8 to 110.8 % for OTC with RSD less than 4.61 % and 91.2 to 104.1 % for DOX with RSD less than 4.18 % (Table 1). As to the proposed fluorescence sensor, the recoveries were 94.7–113.4 %, 95.3–107.4 %, 93.1–112.8 %, 85.8–106.6 % for CTC, TET, OTC and DOX, respectively, and the corresponding RSD was less than 1.36 %, 6.51 %, 3.19 % and 3.93 % (Table 2), showing that the *apt*-NiCoFe-MOF-74 could be served as a sensor for the selective and sensitive detection of TCs in real samples.

4. Conclusion

In this study, a novel and accurate colorimetric/fluorescent dual signal output biosensor depended on the *apt*-NiCoFe-MOF-74 nanozyme with triple-atom site catalyst was proposed for the detection of four TCs with wide linear ranges and low LODs. The proposed labelled biosensing platform in this study improves the accuracy, sensitivity and flexibility of TCs detection and successfully applied in complex food samples with satisfactory recoveries. In addition, this sensor can effectively remove TCs with a high adsorption capacity in food samples. Overall, this approach predicts a fresh direction in the development and manufacture of a new nanozyme sensor, which promising prospects for effectively periodic monitoring and removing contaminants in practical applications.

CRediT authorship contribution statement

Qing Chen: Conceptualization, Funding acquisition, Methodology. **Hongjin Zhang:** Formal analysis, Validation, Writing – original draft. **He Sun:** Data curation, Writing – review & editing. **Yuanzhen Yang:** Investigation, Visualization. **Dandan Zhang:** Investigation, Visualization. **Xin Li:** Funding acquisition. **Lei Han:** Conceptualization, Funding acquisition. **Guannan Wang:** Supervision. **Yang Zhang:** Conceptualization, Funding acquisition, Project administration, Supervision, Writing – review & editing.

Declaration of competing interest

The authors declare that they have no known competing financial interests or personal relationships that could have appeared to influence the work reported in this paper.

Data availability

The authors do not have permission to share data.

Acknowledgments

This work was financially supported by Science Research Foundation of Education Department for Liaoning Province (LJKMZ20221790), Liaoning Applied Basic Research Program (2023JH2/101300079), National Natural Science Foundation of China (Grant No. 22304123), Youth Innovation Team Project for Talent Introduction and Cultivation in Universities of Shandong Province (No. 096-1622002).

Appendix A. Supplementary data

Supplementary data to this article can be found online at https://doi.org/10.1016/j.foodchem.2024.138383.

References

Bing, W., Sun, H., Wang, F., Song, Y., & Ren, J. (2018). Hydrogen-producing hyperthermophilic bacteria synthesized size-controllable fine gold nanoparticles with excellence for eradicating biofilm and antibacterial applications. *Journal of Materials Chemistry B, 6*(28), 4602–4609. https://doi.org/10.1039/c8tb00549d

Du, B., Wen, F., Guo, X., Zheng, N., Zhang, Y., Li, S., & Wang, J. (2019). Evaluation of an ELISA-based visualization microarray chip technique for the detection of veterinary antibiotics in milk. *Food Control, 106*. https://doi.org/10.1016/j.foodcont.2019.106713

Falsafi, T., Mobasheri, F., Nariman, F., & Najafi, M. (2004). Susceptibilities to diffiferent antibiotics of Helicobacter pylori strains isolated from patients at the pediatric medical center of Tehran, Iran. *Journal of Clinical Microbiology, 42*(1), 387-389. https://doi.org/10.1128/jcm. 42.1. 387-389.2004.

Gan, Z., Hu, X., Xu, X., Zhang, W., Zou, X., Shi, J., & Arslan, M. (2021). A portable test strip based on fluorescent europium-based metal-organic framework for rapid and visual detection of tetracycline in food samples. *Food Chemistry, 354*. https://doi.org/10.1016/j.foodchem.2021.129501

Gao, D., Li, B., Huang, X., Liu, X., Li, R., Ye, Z., & Wang, G. (2023). A review of the migration mechanism of antibiotics during struvite recovery from wastewater. *Chemical Engineering Journal, 466*. https://doi.org/10.1016/j.cej.2023.142983

Huang, Y., Ren, J., & Qu, X. (2019). Nanozymes: classification, catalytic mechanisms, activity regulation, and applications. *Chemical Reviews, 119*(6), 4357–4412. https://doi.org/10.1021/acs.chemrev.8b00672

Jiang, D., Ni, D., Rosenkrans, Z. T., Huang, P., Yan, X., & Cai, W. (2019). Nanozyme: New horizons for responsive biomedical applications. *Chemical Society Reviews, 48*(14), 3683–3704. https://doi.org/10.1039/c8cs00718g

Jiao, L., Xu, W., Zhang, Y., Wu, Y., Gu, W., Ge, X., & Guo, S. (2020). Boron-doped Fe-N-C single-atom nanozymes specifically boost peroxidase-like activity. *Nano Today, 35*. https://doi.org/10.1016/j.nantod.2020.100971

Khezerlou, A., Tavassoli, M., Alizadeh Sani, M., Ghasempour, Z., Ehsani, A., & Khalilzadeh, B. (2023). Rapid and sensitive detection of tetracycline residue in food samples using Cr(III)-MOF fluorescent sensor. *Food Chemistry: X, 20*, Article 100883. https://doi.org/10.1016/j.fochx.2023. 100883

Li, H., Chen, Q., Hassan, M. M., Chen, X., Ouyang, Q., Guo, Z., & Zhao, J. (2017). A magnetite/PMAA nanospheres-targeting SERS aptasensor for tetracycline sensing using mercapto molecules embedded core/shell nanoparticles for signal amplification. *Biosensors & Bioelectronics, 92*, 192–199. https://doi.org/10.1016/j.bios.2017.02.009

Li, J., Yao, R., Deng, B., Li, Z., Tuo, K., Fan, C., & Pu, S. (2023). A facile construction of bifunctional core-shell-shell structured magnetic metal-organic frameworks for detection and removal of tetracycline. *Chemical Engineering Journal, 464*. https://doi.org/10.1016/j.cej.2023.142626

Li, Z., Xiao, D., Ge, Y., & Koehler, S. (2015). Surface-functionalized porous lignin for fast and efficient lead removal from aqueous solution. *ACS Applied Materials & Interfaces, 7*(27), 15000–15009. https://doi.org/10.1021/acsami.5b03994

Liang, N., Hu, X., Li, W., Wang, Y., Guo, Z., Huang, X., & Shi, J. (2022). A dual-signal fluorescent sensor based on MoS2 and CdTe quantum dots for tetracycline detection in milk. *Food Chemistry, 378*. https://doi.org/10.1016/j.foodchem.2022.132076

Liang, X., & Han, L. (2020). White peroxidase-mimicking nanozymes: colorimetric pesticide assay without interferences of O-2 and color. *Advanced Functional Materials, 30*(28). https://doi.org/10.1002/adfm.202001933

Liu, B., & Liu, J. (2017). Surface modification of nanozymes. *Nano Research, 10*(4), 1125–1148. https://doi.org/10.1007/s12274-017-1426-5

Liu, B., Zheng, S., Li, H., Xu, J., Tang, H., Wang, Y., & Zhao, X. (2022). Ultrasensitive and facile detection of multiple trace antibiotics with magnetic nanoparticles and core-shell nanostar SERS nanotags. *Talanta, 237*. https://doi.org/10.1016/j.talanta.2021.122955

Mohammed Ameen, S. S., Qasim, F. O., Alhasan, H. S., Hama Aziz, K. H., & Omer, K. M. (2023). Intrinsic dual-state emission zinc-based MOF rodlike nanostructures with applications in smartphone readout visual-based detection for tetracycline: MOF-based color tonality. *ACS Appl Mater Interfaces, 15*(39), 46098–46107. https://doi.org/10.1021/acsami.3c11950

Mohammed Ameen, S. S., Sher Mohammed, N. M., & Omer, K. M. (2023). Ultra-small highly fluorescent zinc-based metal organic framework nanodots for ratiometric visual sensing of tetracycline based on aggregation induced emission. *Talanta, 254*, Article 124178. https://doi.org/10.1016/j.talanta.2022.124178

Pang, Y.-H., Lv, Z.-Y., Sun, J.-C., Yang, C., & Shen, X.-F. (2021). Collaborative compounding of metal?organic frameworks for dispersive solid-phase extraction HPLC?MS/MS determination of tetracyclines in honey. *Food Chemistry, 355*. https://doi.org/10.1016/j.foodchem.2021.129411

Rong, M., Huang, Y., Zhuang, X., Ma, Y., Xie, H., Wu, Y., & Niu, L. (2023). AND logic-gate-based Au@MnO_2 sensing platform for tetracyclines with fluorescent and colorimetric dual-signal readouts. *Sensors and Actuators B-Chemical, 393*. https://doi.org/10.1016/j.snb.2023.134204

Sapsford, K. E., Berti, L., & Medintz, I. L. (2006). Materials for fluorescence resonance energy transfer analysis: Beyond traditional donor-acceptor combinations. *Angewandte Chemie-International Edition, 45*(28), 4562–4588. https://doi.org/10.1002/anie.200503873

Shi, B., Zhang, X., Li, W., Liang, N., Hu, X., Xiao, J., & Shi, J. (2023). An intrinsic dual-emitting fluorescence sensing toward tetracycline with self-calibration model based on luminescent lanthanide-functionalized metal-organic frameworks. *Food Chem, 400*, Article 133995. https://doi.org/10.1016/j.foodchem.2022.133995

Trong Duc, T., Thi Hue, N., & The Binh, N. (2022). Silver nanostructure on ablated silicon wafer prepared via pulsed laser ablation for surface enhanced Raman spectroscopy. *Journal of Raman Spectroscopy, 53*(6), 1039–1047. https://doi.org/10.1002/jrs.6340

Wang, R.-Z., Huang, D.-L., Liu, Y.-G., Zhang, C., Lai, C., Wang, X., & Xu, P. (2020). Synergistic removal of copper and tetracycline from aqueous solution by steam-activated bamboo-derived biochar. *Journal of Hazardous Materials, 384*. https://doi.org/10.1016/j.jhazmat.2019.121470

Wu, J., Wang, X., Wang, Q., Lou, Z., Li, S., Zhu, Y., & Wei, H. (2019). Nanomaterials with enzyme-like characteristics (nanozymes): Next-generation artificial enzymes (II). *Chemical Society Reviews, 48*(4), 1004–1076. https://doi.org/10.1039/c8cs00457a

Xie, B., Yang, X., Zhang, R., Guo, J., Chen, Z., & He, Y. (2021). Hollow and porous Fe3C-NC nanoballoons nanozymes for cancer cell H2O(2) detection. *Sensors and Actuators B-Chemical, 347*. https://doi.org/10.1016/j.snb.2021.130597

Xu, D., Shen, Z., Wang, G., Wei, L., Gao, X., Dong, H., & Guo, Y. (2023). Dual-catalytic colorimetric biosensor based on double-active Fe@Co-N stellate porous carbon and DNAzyme for simultaneous detection of tetracycline antibiotics. *Sensors and Actuators B-Chemical, 376*. https://doi.org/10.1016/j.snb.2022.133024

Xu, Z., Zhao, D., Lu, J., Liu, J., Dao, G., Chen, B., & Pan, X. (2023). Multiple roles of nanomaterials along with their based nanotechnologies in the elimination and dissemination of antibiotic resistance. *Chemical Engineering Journal, 455*. https://doi.org/10.1016/j.cej.2022.140927

Yang, H., Hu, S., Zhao, H., Luo, X., Liu, Y., Deng, C., & Jiang, L. (2021). High-performance Fe-doped ZIF-8 adsorbent for capturing tetracycline from aqueous solution. *Journal of Hazardous Materials, 416*. https://doi.org/10.1016/j.jhazmat.2021.126046

Yang, L., Wang, X., Zhang, F., Yu, L., Bai, B., Zhang, J., & Yang, Y. (2024). Two birds with one stone: A universal design and application of signal-on labeled fluorescent/electrochemical dual-signal mode biosensor for the detection of tetracycline residues in tap water, milk and chicken. *Food Chemistry, 430*. https://doi.org/10.1016/j.foodchem.2023.136904

Yang, Y., Zeng, G., Huang, D., Zhang, C., He, D., Zhou, C., & Ren, X. (2020). In situ grown single-atom cobalt on polymeric carbon nitride with bidentate ligand for efficient photocatalytic degradation of refractory antibiotics. *Small, 16*(29). https://doi.org/10.1002/smll.202001634

Zandieh, M., & Liu, J. (2023). Nanozymes: definition, activity, and mechanisms. *Advanced Materials*. https://doi.org/10.1002/adma.202211041

Zhang, D., Zhang, H., Sun, H., Yang, Y., Zhong, W., Chen, Q., & Zhang, Y. (2023). Differential identification of GSH for acute coronary syndrome using a colorimetric sensor based on nanoflower-like artificial nanozymes. *Talanta, 266*(Pt 1), 124967. https://doi.org/10.1016/j.talanta.2023.124967

Zhang, S., Sun, Q., Liu, X., Li, H., Wang, J., & Chen, M. (2022). Ratiometric fluorescence detection of tetracycline for tetracycline adjuvant screening in bacteria. *Sensors and Actuators B-Chemical, 372*. https://doi.org/10.1016/j.snb.2022.132687

Zhang, Y., Lu, S., Liu, W., Zhao, C., & Xi, R. (2007). Preparation of anti-tetracycline antibodies and development of an indirect heterologous competitive enzyme-linked immunosorbent assay to detect residues of tetracycline in milk. *Journal of Agricultural and Food Chemistry, 55*(2), 211–218. https://doi.org/10.1021/jf062627s

Zhang, Y., Xing, L.-G., Chen, X.-W., & Wang, J.-H. (2015). Nano copper oxide-incorporated mesoporous carbon composite as multimode adsorbent for selective isolation of hemoglobin. *Acs Applied Materials & Interfaces, 7*(9), 5116–5123. https://doi.org/10.1021/am508836m

Zhu, X.-D., Wang, Y.-J., Sun, R.-J., & Zhou, D.-M. (2013). Photocatalytic degradation of tetracycline in aqueous solution by nanosized TiO2. *Chemosphere, 92*(8), 925–932. https://doi.org/10.1016/j.chemosphere.2013.02.066